

Determination of the relative inclination and the viewing angle of an interacting pair of galaxies using convolutional neural networks

Prem Prakash^{1*}, Arunima Banerjee^{1†}, Pavan Kumar Perepu^{1‡}

¹Indian Institute of Science Education and Research, IISER Tirupati, India

Last updated 2020 January 03; in original form 2020 January 03

ABSTRACT

Constructing dynamical models for interacting pair of galaxies as constrained by their observed structure and kinematics crucially depends on the correct choice of the values of the relative inclination (i) between their galactic planes as well as the viewing angle (θ), the angle between the line of sight and the normal to the plane of their orbital motion. We construct Deep Convolutional Neural Network (DCNN) models to determine the relative inclination (i) and the viewing angle (θ) of interacting galaxy pairs, using N-body + Smoothed Particle Hydrodynamics (SPH) simulation data from the GALMER database for training the same. In order to classify galaxy pairs based on their i values only, we first construct DCNN models for a (a) 2-class ($i = 0^\circ, 45^\circ$) and (b) 3-class ($i = 0^\circ, 45^\circ$ and 90°) classification, obtaining F_1 scores of 99% and 98% respectively. Further, for a classification based on both i and θ values, we develop a DCNN model for a 9-class classification ($(i, \theta) \sim (0^\circ, 15^\circ), (0^\circ, 45^\circ), (0^\circ, 90^\circ), (45^\circ, 15^\circ), (45^\circ, 45^\circ), (45^\circ, 90^\circ), (90^\circ, 15^\circ), (90^\circ, 45^\circ), (90^\circ, 90^\circ)$), and the F_1 score was 97%. Finally, we tested our 2-class model on real data of interacting galaxy pairs from the Sloan Digital Sky Survey (SDSS) DR15, and achieve an F_1 score of 78%. Our DCNN models could be further extended to determine additional parameters needed to model dynamics of interacting galaxy pairs, which is currently accomplished by trial and error method.

Key words: methods:data analysis, statistical - catalog:virtual observatory tools - Galaxies:evolution, interaction, kinematics and dynamics

1 INTRODUCTION

According to the modern cosmological paradigm, interacting galaxies constitute the building blocks of the hierarchical structure formation of the universe. It further implies formation of massive or giant galaxies due to the merger of dwarf galaxies, which is corroborated by the abundance of early-type galaxies at higher red-shifts, which are marked by high rates of galaxy interaction. Hence, galaxy interactions facilitate dynamical evolution of galaxies as well as other astrophysical phenomena like morphological galaxy transformations, starbursts, bulge creation, halo formation etc. and only a small fraction of galaxies evolve in isolation via the pathway of secular evolution (See Barnes & Hernquist (1992) for a review).

One of the pioneering studies in the field of interacting galaxies was done by Holmberg (1937). Vorontsov-Vel'yaminov (1959) presented a catalog of 355 pairs of interacting galaxies as observed by the Palomar Observatory Sky Survey (POSS). Arp (1966) attributed the observed peculiarities and distortions present in these galaxies to interactions or mergers, studying a total of 338 inter-

acting pairs. Hibbard et al. (2001) studied interacting galaxies at different wavelengths and published a catalog of peculiar galaxies.

Galaxy interaction is a complex dynamical problem, and therefore not analytically tractable in general. N-body simulation of interacting galaxies was proposed by Holmberg (1941), who simulated the tidal capture in an interacting pair of galaxies. However, this model did not consider alternative scenarios like repeated encounters for the origin of galaxy mergers. Zwicky (1959) first proposed that multiple encounters in close vicinity might lead to total capture or disruption of galaxies. Alladin (1965) showed the capture of spherical galaxies using hyperbolic orbits of encounter. Yabushita (1971) and Tashpulatov (1970) discussed moderate hyperbolic and prolate ellipsoidal orbits for the motion of secondary companion in a merging pair, based on close encounters. Toomre & Toomre (1972) considered parabolic encounters to model the formation of bridge and tails in galaxy mergers.

Most of the simulations mentioned above were low resolution ones, and used only a few hundred particles to construct dynamical models of interacting galaxy pairs (Toomre & Toomre 1972). Further, they mostly modeled the galactic discs as self-gravitating stellar discs though the galactic disc is a gravitationally-coupled, multi-component system of stars, gas and the dark matter halo (see, for example, Bodenheimer (2007)). Construction of a

* E-mail: prmprakash163@googlemail.com

† E-mail: arunima@iisertirupati.ac.in

‡ E-mail: pavankumar@iisertirupati.ac.in

suitable dynamical model for an interacting pair of galaxies with observational constraints strongly hinges on the appropriate choice of initial conditions. The initial conditions may require specification of several dynamical parameters related to mass ratio, energy, spin and orbital geometry. In addition, another set of parameters like viewing directions, length and velocity scales have to be chosen to fit the model results with the observed structure and kinematics (Toomre & Toomre 1972; Chilingarian et al. 2010; Barnes & Hibbard 2009; Barnes 2011; Privon et al. 2013; Mortazavi et al. 2015). As initial conditions are not known a priori, they are currently determined by trial and error method. However, this method is not practicable as the N-body + hydrodynamical simulations are computationally expensive. As such, in our present work, we employ machine learning approaches to determine initial conditions and other parameters for constructing dynamical models for interacting galaxy pairs.

Machine learning techniques have been applied to various problems in astronomy ranging from classifications of stars and galaxies (Weir et al. 1995), optical transients (Cabrera-Vives et al. 2017; Mahabal et al. 2011), galaxy morphology (Dieleman et al. 2015), radio galaxies (Aniyán & Thorat 2017), bar and unbarred galaxies (Abraham et al. 2018) to problems in photometric redshift (Hoyle 2016) and variable starlight (Mahabal et al. 2017). All these methods have been successful in terms of reliability, robustness, accuracy and computation. Aniyán & Thorat (2017) obtained 95% precision for the detection of bent-tailed radio galaxies. Similarly, a precision of 94% was achieved for the classification of barred and un-barred galaxies (Abraham et al. 2018). Recently, Bekki (2019) showed the application of Deep Convolutional Neural Networks (DCNN) on Smoothed Particle Hydrodynamics (SPH) simulation data to determine an optimal orbital geometry of satellite galaxies in galaxy clusters favourable for ram pressure stripping (RPS), and obtained an accuracy of 95%.

We propose the use Deep Convolutional Neural Networks (DCNNs) to determine parameters specifying initial conditions for a dynamical model of an interacting galaxy pair as well as viewing directions to match the model with observations. We use GalMer, an existing database of N-body + Smoothed Particle Hydrodynamical (SPH) simulations of galaxy mergers (Chilingarian et al. 2010) to train the CNN models. In this paper, we develop models to determine the relative inclination (i) between the discs and the viewing angle (θ) which is the angle between the line of sight and the normal to the orbital plane of an interacting pair of galaxies. Finally, we test our model on real images from SDSS DR15. To the best of our knowledge, this is the first instance of application of CNN to this problem (see, for example, Blumenthal et al. (2020))

The rest of the paper is organized as follows. In Section 2, we describe the details of GalMer simulation, in Section 3 data collection and preprocessing. CNN architectures is introduced in Section 4. We discuss experimental results in Section 5 followed by the conclusions in Section 6.

2 GALMER

GalMer is a N-body + SPH galaxy merger simulation with moderate resolution. The galactic model chosen for simulation contains a spherical non-rotating dark-matter halo that may or may not contain a stellar disk, a gaseous disk and a central non-rotating bulge. The

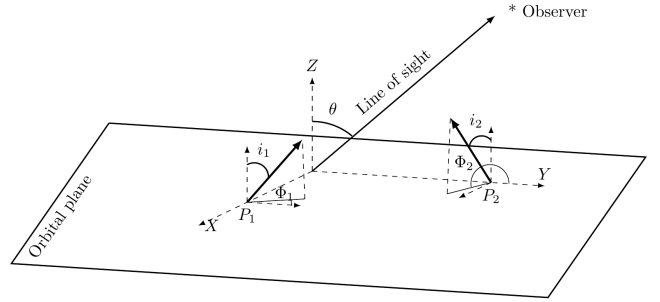


Figure 1. 3D Cartesian coordinate system of GalMer. Inclinations (i_1 and i_2) of the galaxies (P_1 and P_2) are measured with respect to z -axis. Φ_1 and Φ_2 are the corresponding azimuthal angles of galaxies with respect to y -axis and θ is the viewing angle. Relative inclination is given by, $i = i_2 - i_1$. For GalMer, $i_1 = 0$, $\Phi_1 = \Phi_2 = 0$.

galaxies are represented in terms of 1,23,000 particles with total mass distributed among gas, stars and dark matter. It also allows direct comparison between simulation and observation using Virtual Observatory (VO) tools. ¹ framework.

GalMer covers interactions between galaxies of different mass ratios, morphological types, orbit-types, spin types and finally different values of the relative inclination between the discs i . GalMer VO tool allows users to choose different values of the following parameters. The different mass-ratios considered are 1:1, 1:2 and 1:10. The different morphological types included were a giant galaxy (giant elliptical (gE_o), giant lenticular (gS_o), giant spiral (gS_b , gS_a , gS_c , gS_d)) with another giant type (gE_o , gS_o , gS_b , gS_a , gS_c , gS_d) or intermediate-mass (iE_o , iS_o , iS_a , iS_b , iS_d) or dwarf galaxy (dE_o , dS_o , dS_a , dS_b , dS_d). Based on different values of initial distance, pericentric distance and motional energies, 12 different orbit types were chosen. The spin types considered were prograde or retrograde. The relative inclination i between the discs of the interacting galaxies were fixed at any one of the following four values: 0° , 45° , 75° and 90° . Finally, both prograde and retrograde spin types were considered. In order to compare model results with simulation, one can also change (i) angle between the normal to the orbital plane and the line of sight θ between $0^\circ - 90^\circ$ and (ii) the azimuthal angle ϕ subtended by the long axis of the galaxy between $0^\circ - 360^\circ$.

In Fig. 1, we represent a schematic of interaction between two galaxies. In this figure, the interacting pair of galaxies are denoted by P_1 and P_2 . The normal to the orbital plane is taken to coincide with the z -axis of the 3-D cartesian coordinate system. The angle between the spin axis and the axis of orbital motion i.e., z axis for P_1 and P_2 are given by i_1 and i_2 respectively. In addition, azimuthal angles for both the galaxies, Φ_1 and Φ_2 , are taken to be zero. In all Galmer simulations, the first galaxy of the interacting pair is chosen to lie on the orbital plane i.e., $i_1 = 0$. Therefore, the relative inclination between the discs of an interacting pair of galaxy in Galmer simulation is given by $i = i_2 - i_1 = i_2$. The probability of orientation of P_2 between 0 and i_2 is given by $1 - \cos(i_2)$. The viewing angle which is the angle made by line of sight of an observer with normal to the orbital plane, is denoted by θ .

Each galaxy interaction includes 50 to 70 snapshots at an inter-

¹ <http://www.projet-horizon.fr>

Table 1. Distribution of data for two class (0° and 45°) classification

| Data Set | | | |
|------------|----------|------------|---------|
| Class | TRAINING | VALIDATION | TESTING |
| 0° | 5,58,316 | 1,41,524 | 486 |
| 45° | 5,23,733 | 1,32,907 | 456 |

Table 2. Distribution of data for three class (0° , 45° and 90°) classification

| Data Set | | | |
|------------|----------|------------|---------|
| Class | TRAINING | VALIDATION | TESTING |
| 0° | 5,58,316 | 1,41,524 | 486 |
| 45° | 5,23,733 | 1,32,907 | 446 |
| 90° | 6,22,480 | 1,55,120 | 540 |

val of 50 Myr starting from 0 to 2.5/3.5 Gyr. The meta-data produced during interaction can be visualized through the web interface.

3 DATA COLLECTION AND PREPROCESSING

Deep Convolutional Neural Network requires a huge amount of data for training to achieve a desirable accuracy (Duda et al. 2012). In our present work, we restricted ourselves to mass-ratios of 1:1 and interactions between morphological types gS_a and gS_b only i.e., $gS_a - gS_a$, $gS_a - gS_b$ and $gS_b - gS_b$ at their pericentric approach.

We first attempt a 2-class classification based on only one parameter, i : $i = 0^\circ, 45^\circ$. We then implement a 3-class classification with $i = 0^\circ, 45^\circ, 90^\circ$. For each value of i in the above two classification cases, we consider different values of θ : $0^\circ, 20^\circ, 35^\circ, 50^\circ, 65^\circ, 80^\circ$. Finally, we attempt a 9-class classification based on both the parameters, i and θ as follows: $((i, \theta) \sim (0^\circ, 15^\circ), (0^\circ, 45^\circ), (0^\circ, 90^\circ), (45^\circ, 15^\circ), (45^\circ, 45^\circ), (45^\circ, 90^\circ), (90^\circ, 15^\circ), (90^\circ, 45^\circ), (90^\circ, 90^\circ))$. In this case, for each θ , we have also considered a range of values in the neighbourhood, $[\theta - 5^\circ, \theta + 5^\circ]$, to augment the dataset.

We have initially downloaded images of size 450×450 in GIF (Graphics Interchange Format) format, from GalMer website. The total number of obtained images from the above website is only a few hundred in number, which may not be sufficient to train a Deep CNN. As such, we have applied some standard Image Processing operations like contrast enhancement, smoothing etc., on the initial set of images, to increase the size of image database by a factor of 3. As mentioned in (Krizhevsky et al. 2012), we have further augmented the database by rotating all the images, by one degree, 359 times.

After applying the augmentation steps, all the images are scaled to 340×340 size, to reduce computational complexity. In the augmented database, we have used 80% of the total number of images for training and validation, and the remaining 20% for testing.

As mentioned earlier, we have split the database into three sets for training, validation and testing. Validation set can be used to stop the learning process if the training leads to overfitting (Krizhevsky et al. 2012). We have shown the distribution of data into training, validation and testing sets, for two, three and nine classes, in Tables 1, 2, and 3 respectively. In Table 3 for nine classes, each class is denoted by a pair of angles in which first one gives relative inclination of an interacting pair of galaxies while the second one gives the viewing angle. For example, in the first table entry, $(0^\circ, 15^\circ)$, 0° is the relative inclination angle and 15° is the viewing angle.

Table 3. Distribution of data for multi-class classification. Here, each class is denoted by a pair of relative inclination and viewing angles.

| Data Set | | | |
|------------------------|----------|------------|---------|
| Class | TRAINING | VALIDATION | TESTING |
| $(0^\circ, 15^\circ)$ | 3,42,055 | 85,514 | 510 |
| $(0^\circ, 45^\circ)$ | 3,42,055 | 85,514 | 510 |
| $(0^\circ, 75^\circ)$ | 3,42,055 | 85,514 | 510 |
| $(45^\circ, 15^\circ)$ | 3,03,858 | 75,964 | 454 |
| $(45^\circ, 45^\circ)$ | 3,03,858 | 75,964 | 454 |
| $(45^\circ, 75^\circ)$ | 3,03,858 | 75,964 | 454 |
| $(90^\circ, 15^\circ)$ | 3,71,349 | 92,838 | 555 |
| $(90^\circ, 45^\circ)$ | 3,71,349 | 92,838 | 555 |
| $(90^\circ, 75^\circ)$ | 3,71,349 | 92,838 | 555 |

4 CONVOLUTIONAL NEURAL NETWORKS

Convolutional Neural Networks, can be considered as an extension of Artificial Neural Networks (ANNs) to handle 2D data like images. However, the underlying principle for learning is the same, based on error backpropagation (Rumelhart et al. 1986; Hecht-Nielsen 1989) which minimizes the error function, e , shown in equation 1. Here, y is the obtained output of the neuron and \hat{y} is the actual output.

$$e = \frac{1}{2} \|\hat{y} - y\|^2 \quad (1)$$

Initially, CNN has been proposed for handwritten digit recognition by (Lecun et al. 2015) and later it has been applied to other types of data like text, video, speech etc. CNN facilitates automatic feature extraction using a sequence of convolution and pooling layers. Low-level to high-level features are learnt from the input data, in consecutive layers of the network, from left to right. (Zeiler & Fergus 2014; Oquab et al. 2014; Krizhevsky et al. 2012). In the final fully connected output layer, a loss function (Hagenauer et al. 1996) like mean square error, cross entropy etc., is used to optimize parameters of the network.

In our present work, we have used Deep CNN (Krizhevsky et al. 2012; Yosinski et al. 2014) to classify GalMer's synthesized images with various initial interaction inclinations. As our class labels are categorical, we have chosen categorical cross-entropy loss function to optimize network weights. In the literature, DCNN has been widely used in the field of astronomy for different problems like bar detection in galaxies (Abraham et al. 2018; Dieleman et al. 2015), classification of radio galaxies (Aniyan & Thorat 2017), optical transients (Cabrera-Vives et al. 2017), photometric redshifts (Hoyle 2016), variable stars (Mahabal et al. 2017), RPS models (Bekki 2019) etc.

4.1 Network Design

Design of CNN is based on optimizing the tunable parameters like number of layers, kernel size, weights etc. The above design issues have been extensively explored in the literature and some model architectures like AlexNet (Krizhevsky et al. 2012) have been developed, which are made publicly available. In our present work, we have used AlexNet architecture.

4.2 AlexNet

AlexNet design framework, which is shown in Fig 2, contains a total of 12 layers including Convolutional (Conv), Max pooling (MP) and fully connected (FC) layers. Max pooling layers are used to down-sample the input size to reduce the computational complexity.

Table 4. Layer description of AlexNet

| Layer number | Layer type | Kernels/ Pooling windows | Kernel/ Pooling window size | Parameters |
|--------------|-----------------|------------------------------------|-----------------------------|------------|
| 1 | Convolutional | 96 | 11 x 11 | 34944 |
| 2 | Pooling | 96 | 3 x 3 | 34944 |
| 3 | Convolutional | 256 | 5 x 5 | 614656 |
| 4 | Pooling | 256 | 3 x 3 | 614656 |
| 5 | Convolutional | 384 | 3 x 3 | 885120 |
| 6 | Convolutional | 384 | 3 x 3 | 1327488 |
| 7 | Convolutional | 256 | 3 x 3 | 884992 |
| 8 | Pooling | 256 | 3 x 3 | 884992 |
| 9 | Fully Connected | 4096 | NA | 4198400 |
| 10 | Fully Connected | 4096 | NA | 16781312 |
| 11 | Fully Connected | 4096 x 2 | NA | 8194 |
| 12 | Softmax | 2/3/9 (based on number of classes) | | |

All the convolutional layers are followed by Rectified Linear Unit activation (ReLU) (Nair & Hinton 2010) and Normalisation (Norm) functions. The last MP layer is connected to a series of FC layers followed by a final Softmax layer (Gold et al. 1996). These FC layers also use ReLU activation function and the Softmax layer determines the prediction probabilities of the input image in various classes. Input image is classified to a class with highest prediction probability. The model also contains Dropout layers (Srivastava et al. 2014) with 50 percent dropout rates to remove weakly connected neurons in the FC layers. Description of different layers of AlexNet is summarized in Table 4.

4.3 Automated feature extraction

As discussed earlier, CNN automatically extracts low to high level features using kernel windows, directly from the input images. In Fig. 3, we have shown feature maps extracted using one kernel window of each convolutional layer from left to right, for an input image.

5 EXPERIMENTAL RESULTS AND DISCUSSION

We have implemented the AlexNet model in Python using the publicly available Keras library (Chollet et al. 2015) for deep learning. As training involves heavy computations, we have used Intel(R) Core i7-7700 processor with 3.60GHz frequency and 16 GB RAM. The input images are scaled down to 256×256 size and training process takes an average time of around 8 to 10 hours using stochastic gradient algorithm with a learning rate of 0.01 and a decay rate of 1%, for running one full epoch. We have used different number of epochs and steps per epoch for different number of classes, discussed earlier. For two classes, training has been performed with 12 epochs and 12000 steps per epoch. Similarly, 14 epochs with 12000 steps per epoch, and 44 epochs with 16000 steps per epoch, have been used for 3 and 9 classes respectively.

We have also presented learning curves that show the progress of training process, for the above three different cases in Figs. 4, 5 and 6. In these figures, accuracy and loss functions with respect to number of epochs are plotted. It can be observed that the model has achieved an accuracy of 99.9% just after 3 epochs in the case of 2-class classification. If the number of classes is increased to 3 and 9, more number of epochs is required to achieve the same accuracy.

Table 5. Precision, recall and F measures for 2-class classification, 0 and 45 degrees.

| | Precision (%) | Recall (%) | F_1 -Score (%) | Total |
|----------------|---------------|------------|------------------|-------|
| 0° | 0.98 | 1.00 | 0.99 | 478 |
| 45° | 1.00 | 0.97 | 0.99 | 439 |
| Overall | 0.99 | 0.99 | 0.99 | 917 |

Table 6. Number of rejected images from each class in 2-class classification. Rejection threshold is 80%

| Class | Rejection count |
|-------|-----------------|
| 0° | 8 |
| 45° | 17 |

After training the model, we have evaluated the network performance using test data. Performance has been quantified in terms of standard precision, recall and F measures Abraham et al. (2018), whose expressions are discussed below.

$$\text{Precision} = \frac{\text{TP}}{\text{TP} + \text{FP}} \quad (2)$$

$$\text{Recall} = \frac{\text{TP}}{\text{TP} + \text{FN}} \quad (3)$$

$$F_{\beta} = (1 + \beta^2) \cdot \frac{\text{Precision} \times \text{Recall}}{\text{Precision} + \text{Recall}} \quad (4)$$

Here, TP denotes True Positive which is given by the number of correctly classified images in a class. FP and FN denote False Positive and False Negative, which is given by the number of incorrectly classified images (images from first class are classified as second one and vice-versa). In F measure, β determines the weightage of Precision and Recall values. We have set $\beta = 1$ and used F_1 score to give equal weightage for both the values.

We have discussed the performance evaluation using the above measures, for different cases in the following subsections.

Case 1: 2-class classification

In Table 5, we have shown Precision, Recall and F_1 scores for 2-class classification

True positive and false positive rates are plotted on this curve and the area under the curve (AUC) is 0.96. This value is closer to 1, which means that the model has a very good prediction capability.

We have also considered rejections in our performance evaluation. If the highest probability in the Softmax layer, is less than some threshold, which is rejection threshold, the corresponding input image has been rejected. That means, network has not predicted the image with high confidence as determined by the rejection threshold. In our experimentation, we have chosen 80% as the value of rejection threshold. In Table 6, number of rejections for each class are shown. In Fig 7, we have presented confusion matrix that gives statistics on true positives, false positives, true negatives and false negatives. Confusion matrices have been computed excluding the above mentioned rejections.

We have shown a montage of some sample images on which, actual and predicted class labels are overlaid, in Fig. 8.

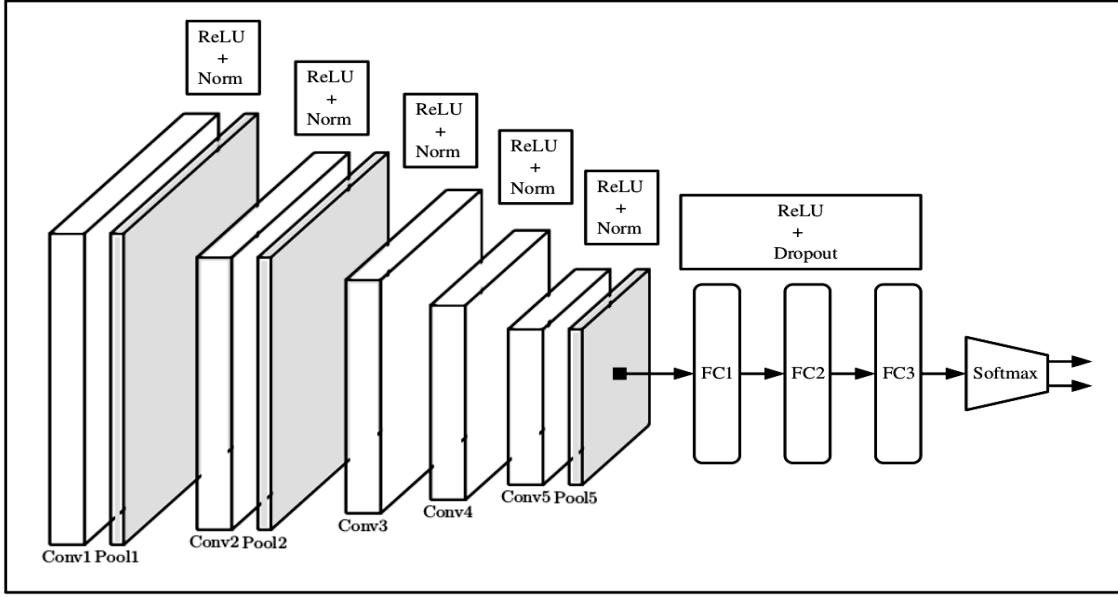


Figure 2. AlexNet architecture

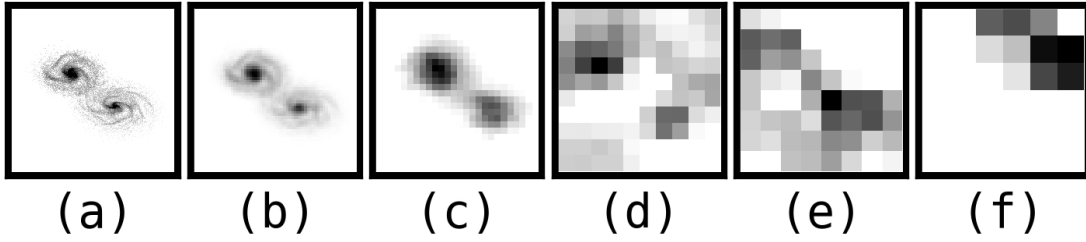


Figure 3. CNN automated feature extraction. (a) Input Image (b)-(f) Feature maps obtained for (a) using one kernel window from each of the five convolutional layers

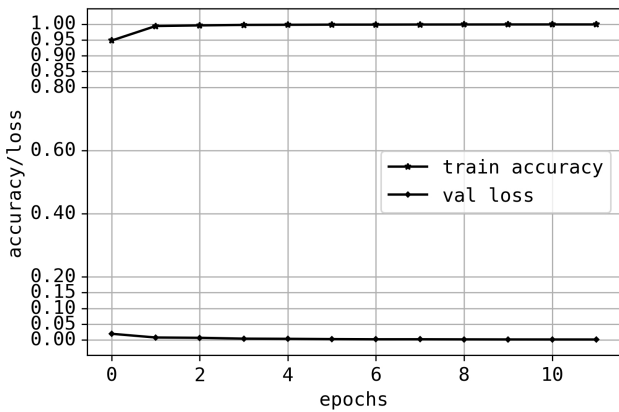


Figure 4. Learning curve for two classes, 0 and 45 degrees.

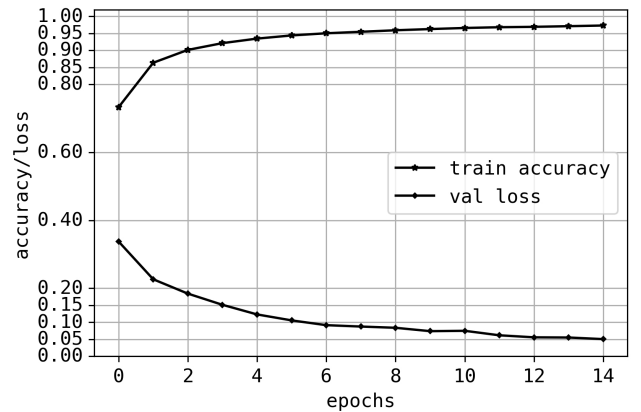


Figure 5. Learning curve for three classes, 0, 45 and 90 degrees.

Case 2: 3-class classification

For this case, precision, recall and F_1 scores are shown in Table 7. We have not plotted ROC curve as it is not straightforward for multi-class classification. Rejected image statistics are shown in

Table 8 and the confusion matrix is presented in Fig. 9. Fig. 10 shows montage of some sample images that include overlaid actual and predicted class labels.

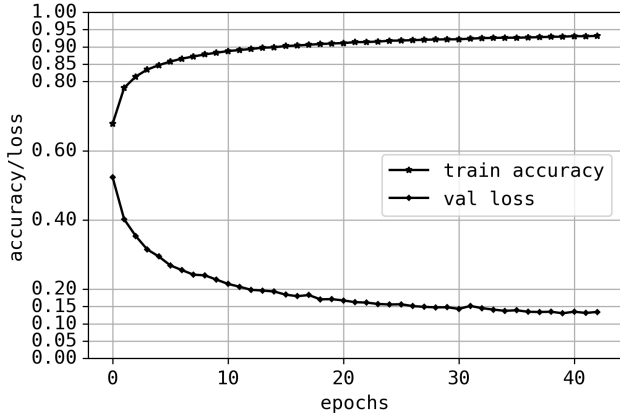


Figure 6. Learning curve for 9 classes (pair of angles).

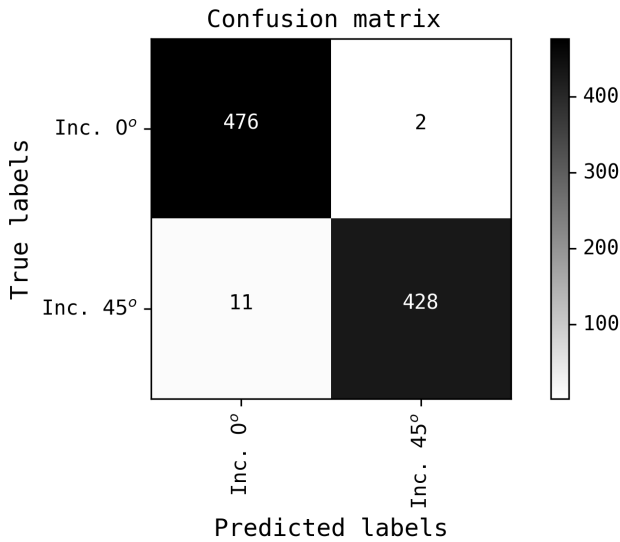


Figure 7. Confusion matrix for 2-class classification, 0 and 45 degrees.

Table 7. Precision, recall and F measures for 3-class classification, 0, 45 and 90 degrees.

| | Precision (%) | Recall (%) | F_1 -Score (%) | Total |
|----------------|---------------|-------------|------------------|-------------|
| 0° | 0.99 | 0.99 | 0.99 | 474 |
| 45° | 0.98 | 0.98 | 0.98 | 410 |
| 90° | 0.97 | 0.97 | 0.97 | 493 |
| Overall | 0.98 | 0.98 | 0.98 | 1377 |

Table 8. Number of rejected images from each class in 3-class classification. Rejection threshold is 80%

| Class | Rejection count |
|-------|-----------------|
| 0° | 12 |
| 45° | 46 |
| 90° | 47 |

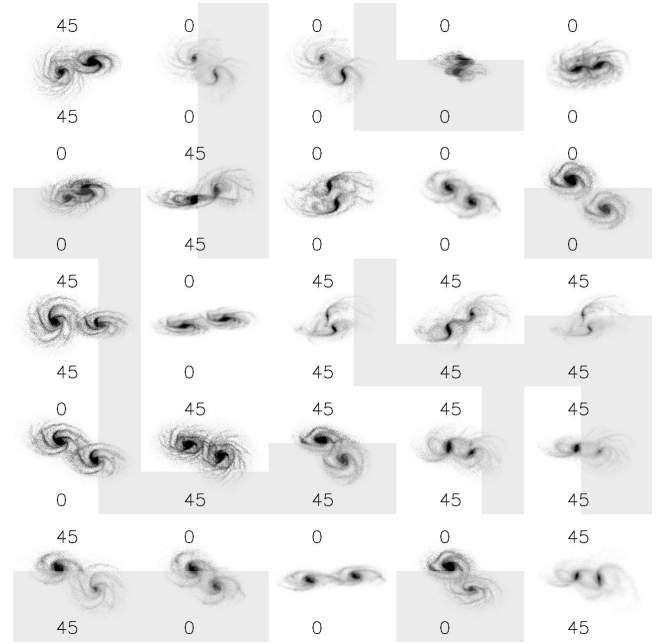


Figure 8. Montage of images for 2-class classification. Top and bottom values on each image represent the actual and the predicted class labels respectively.

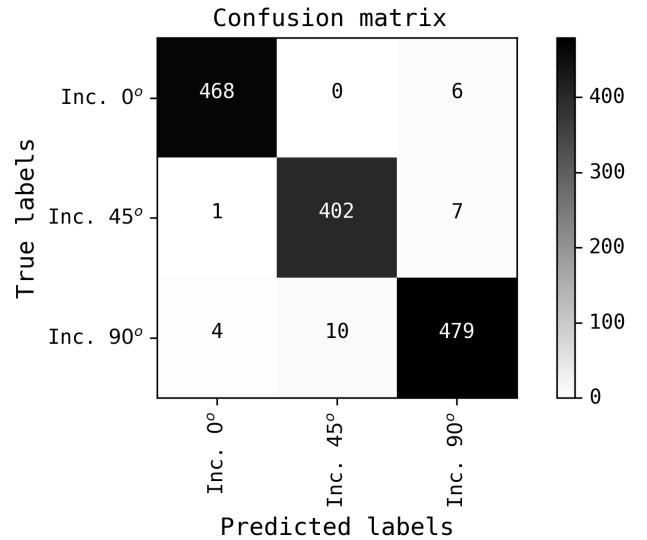


Figure 9. Confusion matrix for 3-class classification, 0, 45 and 90 degrees.

Case 3: 9-class classification

As mentioned earlier, in this case, each class denotes a pair of relative inclination and viewing angles. As the number of classes is increased, prediction accuracy tends to reduce, which can be seen from the values of performance measures in Table 9. This happens if the data may not be sufficient or there may be class imbalance in the data set. As such, we have also reduced the rejection threshold to 70%. The corresponding rejection statistics along with the confusion matrix are shown in Table 10 and Fig. 11 respectively. Finally, montage of some sample images is shown in Fig. 12.

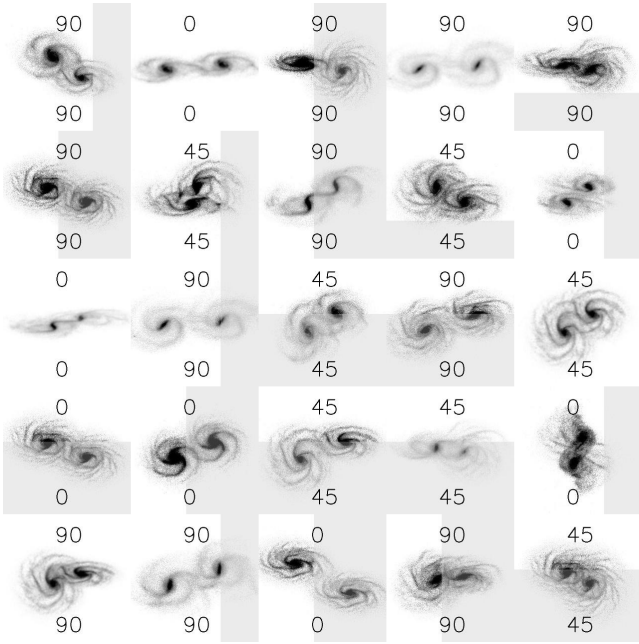


Figure 10. Montage of images for 3-class classification. Top and bottom values on each image represent the actual and the predicted class labels respectively.

Table 9. Precision, recall and F measures for 9-class classification

| | Precision (%) | Recall (%) | F_1 -Score (%) | Total |
|----------------|---------------|-------------|------------------|-------------|
| (0°, 15°) | 1.00 | 1.00 | 1.00 | 509 |
| (0°, 45°) | 0.91 | 0.95 | 0.93 | 435 |
| (0°, 75°) | 0.96 | 0.98 | 0.97 | 476 |
| (45°, 15°) | 0.93 | 0.97 | 0.95 | 430 |
| (45°, 45°) | 0.98 | 0.99 | 0.99 | 431 |
| (45°, 75°) | 0.97 | 0.95 | 0.96 | 400 |
| (90°, 15°) | 0.96 | 0.94 | 0.95 | 504 |
| (90°, 45°) | 0.96 | 0.91 | 0.94 | 469 |
| (90°, 75°) | 1.00 | 0.99 | 0.99 | 542 |
| Overall | 0.97 | 0.97 | 0.97 | 4196 |

Table 10. Number of rejected images from each class in 9-class classification. Rejection threshold is 70%

| Class | Rejection count |
|------------|-----------------|
| (0°, 15°) | 1 |
| (0°, 45°) | 75 |
| (0°, 75°) | 34 |
| (45°, 15°) | 24 |
| (45°, 45°) | 23 |
| (45°, 75°) | 54 |
| (90°, 15°) | 51 |
| (90°, 45°) | 86 |
| (90°, 75°) | 13 |

We have analyzed several factors that may cause false predictions which generate non-zero off-diagonal values in the confusion matrices. The major factors that can affect the morphological signatures at the close encounter epoch, are relative inclination of the orbital plane of merging pairs, type of orbit (including the total energy of pair and the relative pericentric distances) and the spin type (prograde or retrograde) of galaxies. Model performance is affected

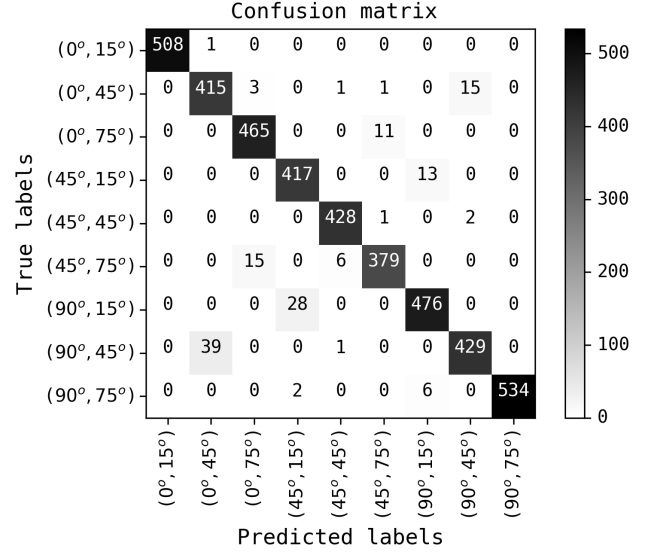


Figure 11. Confusion matrix for 9-class classification.

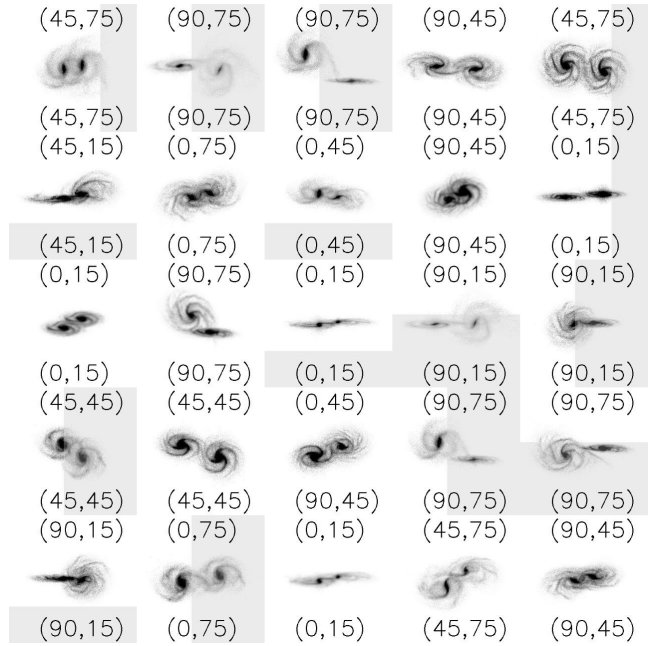


Figure 12. Montage of images for 9 class classification. Actual and predicted classes are shown in the top and bottom regions of the image, respectively.

if there are anomalies in the data on spin and orbit combination for merging pairs.

Results on real data

As mentioned earlier, we have trained our CNN model using simulated data from GalMer. We have also applied the trained model for two classes, on real data from Sloan Digital Sky Survey (SDSS) Data Release 15 (DR15). DR15 contains all data released upto July 2017 which is the third release of fourth phase of SDSS-IV and it also contains all data from the earlier releases.

Table 11. Galaxy data for 0° relative inclination angle

| Obj_Id | RA | DEC | i_1 | i_2 | PA_1 | PA_2 | i |
|---------------------|--------|-------|-------|-------|--------|--------|-------|
| J15265746+1009004 | 231.74 | 10.15 | 61.3 | 61.4 | 109.7 | 109.1 | 0.54 |
| J14312747+1324353 | 217.86 | 13.41 | 59 | 57.7 | 10.6 | 11.1 | 1.37 |
| J00515274-0900558 | 12.97 | -9.02 | 65.4 | 67.4 | 143.2 | 145.6 | 2.97 |
| J105953.07+432208.2 | 164.97 | 43.37 | 90 | 90 | 107.1 | 110.6 | 3.50 |
| J131530.95+620745.0 | 198.87 | 62.13 | 82.8 | 80.5 | 110.8 | 102.6 | 8.43 |
| J01324722-0825268 | 23.20 | -8.42 | 59.1 | 59.6 | 46.8 | 36.1 | 9.22 |
| J092229.43+502548.7 | 140.62 | 50.43 | 90 | 90 | 77.2 | 86.9 | 9.70 |
| J083802.75+075326.2 | 129.51 | 7.89 | 90 | 90 | 107.2 | 117.6 | 10.40 |
| J13485859+1458311 | 207.24 | 14.98 | 77.8 | 67.6 | 20.7 | 25.9 | 11.34 |
| J08042267+4038554 | 121.09 | 40.65 | 35.7 | 39.7 | 78.6 | 98.4 | 12.70 |
| J104949.74+325903.1 | 162.46 | 32.98 | 66.4 | 57.8 | 29.4 | 40.5 | 13.03 |
| J15013746+2530564 | 225.41 | 25.52 | 52.5 | 56.8 | 139.2 | 154.4 | 13.10 |
| J15063018+6035402 | 226.63 | 60.59 | 50.7 | 40.5 | 29.7 | 17.1 | 13.57 |
| J130354.72-030631.6 | 195.98 | -3.11 | 90 | 90 | 157.7 | 171.8 | 14.10 |
| J134814.33+152538.5 | 207.06 | 15.43 | 45.5 | 42.5 | 41 | 61.9 | 14.78 |

Table 12. Galaxy data for 45° relative inclination angle

| Obj_Id | RA | DEC | i_1 | i_2 | PA_1 | PA_2 | i |
|---------------------|--------|-------|-------|-------|--------|--------|-------|
| J13563793+5314130 | 209.16 | 53.24 | 64.4 | 90 | 15.8 | 41.9 | 35.92 |
| J120423.84+275616.5 | 181.10 | 27.94 | 59.5 | 45.9 | 179.4 | 136.9 | 35.96 |
| J133958.60+005006.7 | 204.99 | 0.84 | 34.2 | 69.9 | 177.9 | 166.4 | 36.73 |
| J125322.35-002542.7 | 193.34 | -0.43 | 46 | 72.7 | 55 | 24.6 | 36.97 |
| J11483797+5656514 | 177.16 | 56.95 | 40.8 | 32.1 | 81.6 | 147.9 | 38.66 |
| J10174066+2047438 | 154.42 | 20.80 | 42.2 | 63.8 | 169.8 | 126.4 | 40.09 |
| J11263223+4102333 | 171.63 | 41.04 | 41 | 38.5 | 158.2 | 91.5 | 41.22 |
| J120439.56+525726.6 | 181.16 | 52.95 | 57.3 | 67.7 | 41.6 | 87.9 | 42.02 |
| J13442640-0224196 | 206.11 | -2.41 | 67.9 | 82.4 | 34.2 | 76 | 42.74 |
| J08281380+1741338 | 127.06 | 17.69 | 37.2 | 28.9 | 117.6 | 31.2 | 44.30 |
| J133614.07-010217.3 | 204.05 | -1.03 | 70.9 | 36.1 | 152.6 | 115 | 45.13 |
| J14165155+5410476 | 214.21 | 54.18 | 53.6 | 90 | 56.9 | 87.3 | 46.03 |
| J08333938+5152066 | 128.41 | 51.87 | 90 | 38.9 | 2.8 | 3.8 | 51.11 |
| J08513476+3916087 | 132.89 | 39.27 | 58.6 | 52.3 | 97.7 | 160.5 | 51.15 |
| J09543272+5633246 | 148.64 | 56.56 | 90 | 51 | 106.8 | 66.2 | 53.84 |

SDSS Casjobs ² can be used to fetch image data based on right ascension (RA) and declination (DEC) parameters, using SQL queries from different releases.

To generate the data, we have selectively labelled the images based on user voting such that the manual labelling for at least 80 percent of the users should be consistent. The selected data has then been visually inspected for quality and application feasibility. We have used HyperLEDA ³, a database for galaxies and cosmology, to fetch the individual inclination and position angle for each galaxy in the interacting pair. As discussed in HyperLEDA, position angle is the angle subtended by longest axis of galaxy with respect to celestial North and it is measured in terms of 0 to 180 degrees from North to East. Relative inclination angles (i) have been computed using Eq 5, based on the individual inclinations (i_1 and i_2) and position angles (say, PA_1 and PA_2) of the two galaxies in a pair. In GalMer, position angle is zero as the view is considered from the top onto the orbital plane. We have used these angles to assign class labels to images. We have also shown the above parameters along with SDSS object ID (**Obj_Id**) for a few galaxy samples with 0° and 45° inclination angles in 11 and 12 respectively. It can be observed from these tables that we have considered relative inclination values in an interval of $\pm 15^\circ$ around the exact angles (0° or 45°), as it may

Table 13. Precision, recall and F measures for 2-class (0° and 45°) classification on real data.

| | Precision (%) | Recall (%) | F_1 -Score (%) | Total |
|----------------|---------------|------------|------------------|-------|
| 0° | 0.82 | 0.69 | 0.75 | 13 |
| 45° | 0.75 | 0.86 | 0.80 | 14 |
| Overall | 0.78 | 0.78 | 0.78 | 27 |

not be possible to get more samples only with the exact ones.

$$\cos(i) = \sin(i_1) \sin(i_2) \cos(PA_1) \cos(PA_2) + \sin(i_1) \sin(i_2) \sin(PA_1) \sin(PA_2) + \cos(i_1) \cos(i_2) \quad (5)$$

As these images are taken from real database, noise may be present in them. So, we have applied median filter on the images, to eliminate noise and later scaled them to a size of 340×340 pixels. We have tested the final obtained data on our earlier trained binary classification model and the corresponding precision, recall and F_1 scores are shown in Table 13. From the confusion matrix shown in Fig 13, it can be observed that out of total 30 images, 22 are correctly predicted with a confidence level of 80 percent (rejection threshold). Finally, montage of a few sample real images are shown in Fig 14.

² <http://skyserver.sdss.org/CasJobs/>

³ <http://leda.univ-lyon1.fr/>

Table 14. Number of rejected images from each class in 2-class real data classification. Rejection threshold is 80%

| Class | Rejection count |
|-------|-----------------|
| 0° | 2 |
| 45° | 1 |

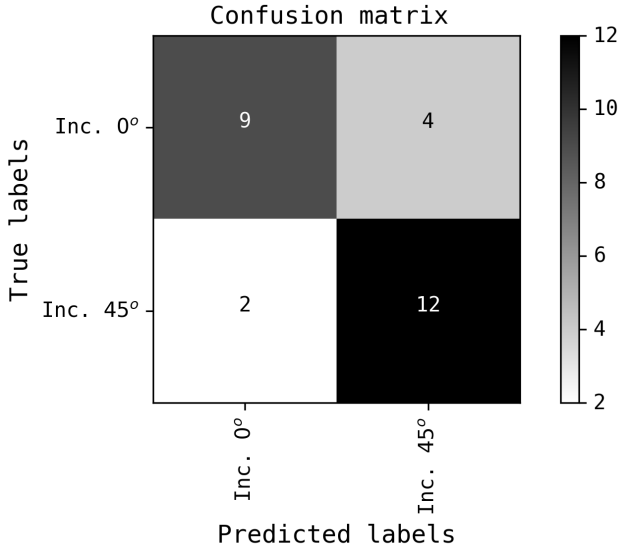


Figure 13. Confusion matrix for 2-class classification on real data.

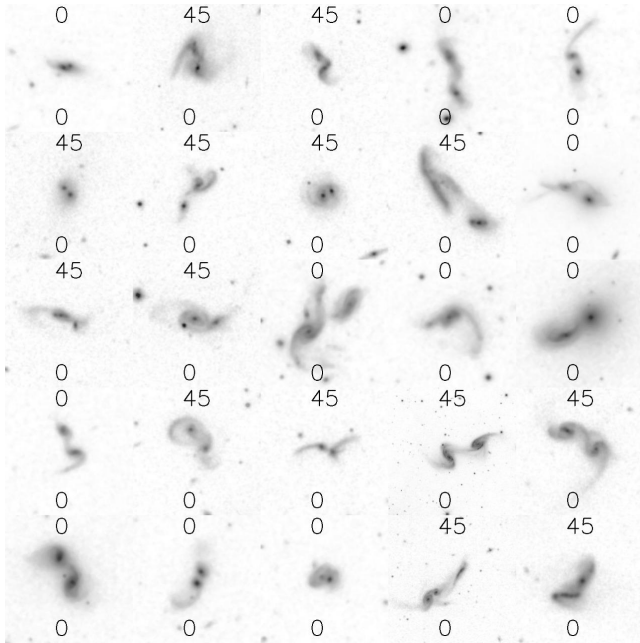


Figure 14. Montage of real images for 0 and 45 degrees interactions. The top and bottom values on each image represent the actual and the predicted class labels.

6 CONCLUSIONS

We have demonstrated the application of Deep Convolutional Neural Networks (DCNN) in determining the fundamental parameters governing dynamical modelling of interacting galaxy pairs: the relative inclination i between their discs and the viewing angle θ which is the angle between the line of sight and the normal to the orbital plane. We have used images from GALMER N-body + SPH simulation of 1:1 merger of interacting galaxy pairs at their pericentric approach for training our DCNN models. The training sample represents well galaxy interactions between different morphological types ($gS_a - gS_a$, $gS_a - gS_b$ and $gS_b - gS_b$), also spanning a large range of parameters characterizing the dynamical models as given by the different orbit and spin types. Our DCNN model for a (a) 2-class ($i \sim 0^\circ, 45^\circ$) (b) 3-class ($i \sim 0^\circ, 45^\circ$ and 90°) and (c) 9-class classification ($(i, \theta) \sim (0^\circ, 15^\circ), (0^\circ, 45^\circ), (0^\circ, 90^\circ), (45^\circ, 15^\circ), (45^\circ, 45^\circ), (45^\circ, 90^\circ), (90^\circ, 15^\circ), (90^\circ, 45^\circ), (90^\circ, 90^\circ)$) classification obtained F_1 scores of 99%, 98% and 97% respectively. We also tested our 2-class model on real data from SDSS DR15 and achieved an F_1 score of 78%. Our DCNN models thus can be employed to determine the parameters specifying the initial conditions of dynamical models of galaxy interactions, which is otherwise obtained by an iterative method.

ACKNOWLEDGEMENTS

We would like to thank Dr. Arun K. Aniyam and Prof. Francoise Combes for useful suggestions and discussion. We would also like to acknowledge DST-INSPIRE Faculty Fellowship (IFA14/PH-101) for supporting this research.

REFERENCES

- Abraham S., Aniyam A. K., Kembhavi A. K., Philip N. S., Vaghmare K., 2018, *MNRAS*, **477**, 894
- Alladin S. M., 1965, *ApJ*, **141**, 768
- Aniyam A. K., Thorat K., 2017, *ApJS*, **230**, 20
- Arp H., 1966, *ApJS*, **14**, 1
- Barnes J. E., 2011, *MNRAS*, **413**, 2860
- Barnes J. E., Hernquist L., 1992, *ARA&A*, **30**, 705
- Barnes J. E., Hibbard J. E., 2009, *The Astronomical Journal*, **137**, 3071
- Bekki K., 2019, *MNRAS*, **485**, 1924
- Blumenthal K. A., et al., 2020, *MNRAS*, **492**, 2075
- Bodenheimer P., ed. 2007, *Numerical Methods in Astrophysics: An Introduction*
- Cabrera-Vives G., Reyes I., Förster F., Estévez P. A., Maureira J.-C., 2017, *ApJ*, **836**, 97
- Chilingarian I. V., Di Matteo P., Combes F., Melchior A. L., Semelin B., 2010, *A&A*, **518**, A61
- Chollet F., et al., 2015, Keras, <https://keras.io>
- Dieleman S., Willett K. W., Dambre J., 2015, *MNRAS*, **450**, 1441
- Duda R. O., Hart P. E., Stork D. G., 2012, *Pattern classification*. John Wiley & Sons
- Gold S., Rangarajan A., et al., 1996, *Journal of Artificial Neural Networks*, **2**, 381
- Hagenauer J., Offer E., Papke L., 1996, *IEEE Transactions on information theory*, **42**, 429
- Hecht-Nielsen R., 1989, in *Neural computers*. Springer, pp 445–453
- Hibbard J. E., van Gorkom J. H., Rupen M. P., Schiminovich D., 2001, *An HI Rogues Gallery*. p. 657
- Holmberg E., 1937, *Annals of the Observatory of Lund*, **6**, 1
- Holmberg E., 1941, *ApJ*, **94**, 385
- Hoyle B., 2016, *Astronomy and Computing*, **16**, 34

- Krizhevsky A., Sutskever I., Hinton G. E., 2012, in Advances in neural information processing systems. pp 1097–1105
- Lecun Y., Bengio Y., Hinton G., 2015, *Nature*, **521**, 436
- Mahabal A. A., et al., 2011, Bulletin of the Astronomical Society of India, **39**, 387
- Mahabal A., Sheth K., Gieseke F., Pai A., Djorgovski S. G., Drake A., Graham M., the CSS/CRTS/PTF Collaboration 2017, arXiv e-prints, p. [arXiv:1709.06257](https://arxiv.org/abs/1709.06257)
- Mortazavi S. A., Lotz J., Barnes J. E., 2015, in American Astronomical Society Meeting Abstracts #225. p. 231.03
- Nair V., Hinton G. E., 2010, in Proceedings of the 27th International Conference on International Conference on Machine Learning. ICML'10. Omnipress, Madison, WI, USA, p. 807–814
- Oquab M., Bottou L., Laptev I., Sivic J., 2014, in The IEEE Conference on Computer Vision and Pattern Recognition (CVPR).
- Privon G. C., Barnes J. E., Evans A. S., Hibbard J. E., Yun M. S., Mazzarella J. M., Armus L., Surace J., 2013, *ApJ*, **771**, 120
- Rumelhart D. E., Hinton G. E., Williams R. J., 1986, *nature*, 323, 533
- Srivastava N., Hinton G., Krizhevsky A., Sutskever I., Salakhutdinov R., 2014, *Journal of Machine Learning Research*, 15, 1929
- Tashpulatov N., 1970, *Soviet Ast.*, **13**, 968
- Toomre A., Toomre J., 1972, *ApJ*, **178**, 623
- Vorontsov-Vel'yaminov B. A., 1959, in Proceedings of the Sixth Conference of Questions of Cosmology. p. 20
- Weir N., Fayyad U. M., Djorgovski S., 1995, *AJ*, **109**, 2401
- Yabushita S., 1971, *MNRAS*, **153**, 97
- Yosinski J., Clune J., Bengio Y., Lipson H., 2014, in Advances in neural information processing systems. pp 3320–3328
- Zeiler M. D., Fergus R., 2014, in European conference on computer vision. pp 818–833
- Zwicky F., 1959, *Handbuch der Physik*, **53**, 373

This paper has been typeset from a $\text{\TeX}/\text{\LaTeX}$ file prepared by the author.